Acta Materialia xxx (xxxx) 121645

Contents lists available at ScienceDirect

Acta Materialia

journal homepage: www.elsevier.com/locate/actamat

Origin of twinning mode hierarchy in NiTi – A critical understanding

Daegun You [a], Ahmed Sameer Khan Mohammed [a], Minoru Nishida [b], Huseyin Sehitoglu [a, *]

[a] Department of Mechanical Science and Engineering, University of Illinois at Urbana-Champaign, 1206 W Green St, Urbana, IL 61801, USA
[b] Faculty of Engineering Sciences, Kyushu University, 6-1, Kasuga-koen, Kasuga, Fukuoka 816-8580, Japan

ARTICLE INFO

Keywords:
Shape memory alloy
Type-I twin
Twin boundary
Lattice offset
Atomic shuffle

ABSTRACT

Experimental evidence has universally demonstrated the coexistence of $\left\{11\bar{1}\right\}$ Type-I twins and $\langle 011\rangle$ Type-II twins—defined as lattice-invariant deformation—within the same habit plane variant of the B19' martensite in Ni-Ti alloys. This coexistence is unexpected because, although $\left\{11\bar{1}\right\}$ Type-I twins represent a valid solution derived from the phenomenological theory of martensite crystallography, they are not conjugate to the experimentally dominant $\langle 011\rangle$ Type-II twins. A clear explanation for the widespread occurrence of $\left\{11\bar{1}\right\}$ Type-I twinning mode has been elusive. This study shows calculations of twin boundary (TB) energies for both twinning modes in Type-I and found that $\left\{11\bar{1}\right\}$ twinning is favored over $\{011\}$ since the TB energy is much lower by a factor of three. The accurate determination of TB energy requires ab-initio calculations because the classical interatomic potentials miss the correct positioning of the lattice-motif points. High-resolution experimental images at the atomic level confirm the positioning of Ni and Ti atoms and agree precisely with our calculations. Furthermore, experimental electron diffraction images and simulated images agree only when the correct interface is constructed as in this study. With the correct offsets, further shear and shuffles establish twin nucleation and migration barriers that elucidate a preference for $\left\{11\bar{1}\right\}$ Type-I twinning mode in NiTi alloys. In summary, the current study employs Density Functional Theory (DFT) and three recently proposed Molecular Dynamics (MD) potentials to gain further insights into twinning in NiTi, while also serving as a critical evaluation of the proposed MD models.

1. Introduction

Shape memory alloys (SMAs) recover large strains under thermo-mechanical loadings [1–3], making them valuable for bio-medical, robotics, and structural applications [4–7]. Their unique properties arise from the reversible phase transformation from austenite to martensite [8,9]. Research on SMAs necessitates a solid understanding of the internal twinning in martensite which accommodates large strains and minimizes the Gibbs free energy [10]. Under stress, the preferable twin variants grow, and ultimately, the martensite detwins reaching a single crystal state. Considerable literature exists on the SMA mechanical response, especially on NiTi, but a full understanding of twinning deformation [11,12] remains elusive. Many of the phenomena that NiTi exhibits, such as elastic moduli evolution [13], asymmetric stress-strain behavior [11], and dislocation slip emission [14–16], can be better understood through a deeper insight into twinning.

Type-II twinning energy barriers for twinning [11,12,17–21] have been studied in previous work, but there has been less focus on Type-I twinning despite its significance [22,23]. In NiTi alloy B19' martensite, $\left\{11\bar{1}\right\}$ Type-I twins are widely recognized [23–29]. This twin has two forms. One is a spear-shaped variant accommodation twin that exists at the V-shaped interface, which is the smallest unit of the self-accommodation structure composed of two habit plane variants (HPVs) [23,27,28]. The other is a twin that coexists with a $\langle 011\rangle$ Type-II twin, which is a primary lattice-invariant-shear (LIS) or -deformation within the same HPV [22,23]. The significance and necessity of the former have been clarified through analyses based on phenomenological theory of martensite crystallography (PTMC) and geometrically nonlinear

* Corresponding author.
E-mail address: huseyin@illinois.edu (H. Sehitoglu).

https://doi.org/10.1016/j.actamat.2025.121645
Received 4 August 2025; Received in revised form 7 October 2025; Accepted 16 October 2025
1359-6454/

theory [30]. The latter is the focus of this paper, and the reasons for this are explained below.

A specific question on twinning is whether $\{011\}$ Type-I or $\left\{11\bar{1}\right\}$ Type-I is preferred. The $\{011\}$ Type-I is conjugate to Type-II but is rarely observed. Instead, $\left\{11\bar{1}\right\}$ Type-I dominates the experimental observations. Why? Currently, the interfacial energies, twin nucleation and migration barriers for Type-I twinning modes are not well understood. This is because the atom positions at twin boundaries do not exhibit mirror symmetry, and there are offsets at boundaries. Furthermore, the twin migration analysis must begin with the initial lattice interface, including offsets, and then impose internal shears and shuffles to advance the twin. This study is the first to examine Type-I twin construction while fully considering lattice offsets at the interface and the formation of minimal interfacial energies. High-resolution microscopy of atomic positions and electron diffraction images confirm the lattice-motif positions of Ni and Ti at the interface, revealing corrugated interfaces that previous studies had overlooked, that deviate from perfect mirror reflection, thereby supporting the primary objective of this work. Electron diffraction patterns from the experiments and simulations agree only in the case of correct positioning of atoms at the interface.

In summary, Type-I TB is a crucial interface and has a unique irrational twinning shear direction. The general structural characteristics of this twin differ significantly from the Type-II twin interface. The energy of Type-I interface is determined using ab-initio Density Functional Theory (DFT) calculations with the construction of different configurations. The findings indicate that the energy-minimal atomic structure requires the identification of a "lattice-offset," which is complex and not known a priori. In addition to the DFT calculations, we established the twin boundary energies with three recently proposed Molecular Dynamics (MD) potentials [31–33] and discuss the efficacy of these potentials.

In addition to their technological importance, TB structures provide valuable scientific insights by demonstrating a range of behaviors in terms of interface types. They serve as benchmarks for understanding grain boundaries and other types of crystalline interfaces. The classical theory of deformation twinning [34,35] is well known, but a comprehensive understanding of the atomic positions and the energies associated with twin interfaces [15,36,37] remains incomplete. In the following subsections, we first introduce and define the twinning modes and their importance in NiTi martensite in detail.

1.1. Twinning modes in NiTi martensite

Three major orientation relationships were defined by presented here in brief for the reader's convenience and this is illustrated in Fig. 1:

i. Type-I twins: The lattices of the twin variants are related by mirror symmetry with the TB being the mirror plane.
ii. Type-II twins: The lattices of the twin variants are related by 180° rotational symmetry about an axis along the direction of twinning shear.
iii. Compound twins: The lattices of the twin variants obey both symmetries defining Type-I and Type-II twins.

The nature of symmetry obeyed by the twin-variants in Type-I and Compound twinning modes allow their TBs to exhibit rational Miller-index identities, defining an unambiguous crystallographic plane for the TB.

The presence and mobility of Type-I twins has important implications to mechanical behavior of SMAs. The mobility of the TB influences the ease of TB migration and detwinning, impacting the functional performance of ferromagnetic SMAs such as NiMnGa [38,39]. Therefore, a clear understanding of the structure, topology, and energy of Type-I TBs is a necessary precursor to assess their influence on mechanical behavior of SMAs. Previously, significant focus has been attributed to the NiTi system, where the scientific and commercial success of the material's functionality fostered strong prior research on experimental and modeling fronts directed toward understanding its Type-II TB [15,17,23,26,40–44]. This study examines the Type-I interfaces and determine the energies of the interface. By doing so, the goal is to develop a general framework to model Type-I TBs in general and to reveal novel characteristics of the irrational TB that have broader relevance beyond a given specific alloy system. Experimental evidence of Type-I TBs in the NiTi SMAs can be found elsewhere [23–25,27–29,45–47].

In Table 1, we summarize the observations of possible twinning modes in NiTi martensite. Martensitic phases generally exhibit high yield stresses for slip [50] in SMAs and deform through internal detwinning or TB migration. Four evident twinning modes in the B19' phase are the $\left\{11\bar{1}\right\}$ Type-I, $\langle 011\rangle$ Type II, $\{100\}$ and $\{001\}$ Compound twinning modes, the first of which is the twinning mode of focus in this study. The martensite NiTi is internally twinned in various modes by multiple HPVs to reduce transformation stress. Those HPVs by PTMC are adjacent to each other with opposite shear direction (i.e., LIS), known as a self-accommodated state [3,27,28,30]. Among the multiple twin modes, $\langle 011\rangle$ Type-II twins are the most common [40,51] for solutionized cases, while the interaction of Type-II twins produce various Type-I interfaces [27,28,30]. The (001) twins exist in the aged alloys [48,52] or in fine grained NiTi [53,54]. Upon application of stress, the transformation twin boundaries migrate and this typically occurs at low stresses. Deformation twins are activated at higher strains. Higher order twins such as $\left(\bar{2}01\right)$ can also form [55] but they may not be recoverable upon unloading or upon heating.

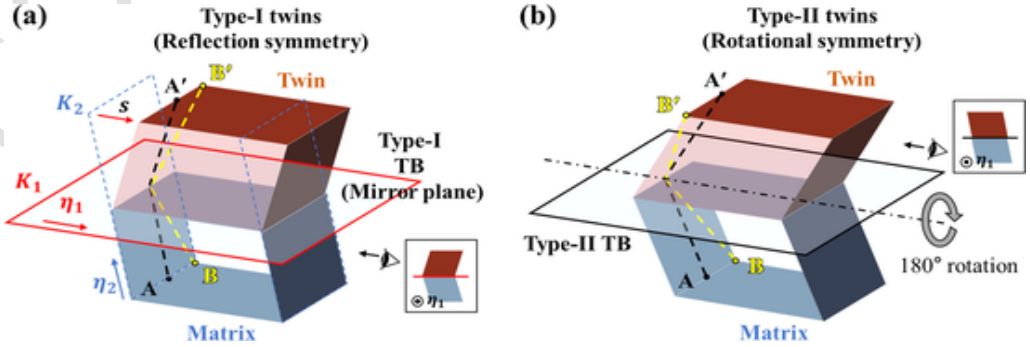

Fig. 1. Classification of (a) Type-I and (b) Type-II twins in NiTi martensite. Definition of twinning elements is noted in (a). Inset schematic is side view of each type along twinning direction.

Table 1
Twinning modes in NiTi martensites found in experiments and/or theory.

Possible twins by theory (Indexed in parent B2 lattice)	Observed Twins in experiments (Indexed in martensite B19′ lattice)	Experimental and Theoretical Observations
$\{100\}_C\langle 011\rangle_C$ Compound-1	$(100)_M[001]_M$ Compound [3,22,23,29,46]	Yes-Previous studies
$\{011\}_C\langle 100\rangle_C$ Compound-2	$(001)_M[100]_M$ Compound [22–25,29,46]	Yes-Previous studies
$\{100\}_C\langle 0\ 0.7864\ \bar{1}\rangle_C$ Type-I.1	$(011)_M\left[1.5727\ 1\ \bar{1}\right]_M$ Type-I [22–24]	Yes-*This study*
$\{1\bar{1}0\}_C\langle 1\ 1\ 0.3230\rangle_C$ Type-I.2	$\left(\bar{1}11\right)_M[0.5404\ 0.4596\ 1]_M$ Type-I [3,24,48]	Yes-*This study*
$\{1\bar{1}0\}_C\langle 1\ 1\ 2.7008\rangle_C$Type-I.3	$(111)_M\left[\overline{1.5117}\ 0.5117\ 1\right]_M$ Type-I [24,29]	Yes-No
$\{0.7205\ 0\ \bar{1}\}_C\langle 010\rangle_C$ Type-II.1	$\left(0.7205\ 1\ \bar{1}\right)_M[011]_M$ Type-II [3,23,25–29,40–43,46,48,49]	Yes-Previous studies
$\{\bar{1}\ 1\ 0.4953\}_C\langle 110\rangle_C$ Type-II.2	Not Observed	No-No
$\{1\ 1\ 3.0495\}_C\langle\bar{1}10\rangle_C$ Type-II.3	Not Observed	No-No

Experimentally, Type-II type twins are most commonly observed for solutionized NiTi and rearrange during the stress plateau of the martensite deformation and form Type-I twins at interfaces [29,42,43]. The study of Type-II twins in NiTi martensite has remained a topic of considerable debate regarding its unique interface morphology recently [26,40,42,43,46]. Specifically, phenomenological models [56–58] widely consider the twinning plane as irrational [34], i.e., $\left(0.7205\ 1\ \bar{1}\right)$, while high resolution TEM analyses [41–43] suggest a rational yet stepped geometry. The origin of rather unusual boundary geometry is attributed to a need to minimize the total interfacial energy [42,59]. Both shear and shuffle displacements contribute to this type of twinning [17]. The twinning energy landscapes for the Type II twins and the (001) and (100) modes (based on [18]) with different barriers 7.6 mJm^{-2} and 41 mJm^{-2} have been established. Similar studies on Type-I twinning mode are missing.

In the previous studies, theoretically, Type-II twinning mode in NiTi martensite has been accurately investigated with respect to its generalized planar fault energy (GPFE) via DFT [15,17]. Since the GPFE includes TB energy but also nucleation-migration barriers, the different twinning modes can be directly compared in both aspects. Theoretical explanation of Type-I twinning modes is not well established in that aspect since it requires an accurate determination of TB interface. Although a recent study represents TB energies of Type-I twinning modes [60], these do not explain the observation frequencies over different twinning modes. The hierarchy of twinning modes should be explained with respect to their nucleation and intrinsic stabilization where the TB has formed, which can be captured in GPFE.

1.2. Hierarchy of twinning modes

Type-1 twinning modes ($\{011\}$ and $\left\{11\bar{1}\right\}$), namely Type-I.1 and Type-I.2, which we focus on in this study, possess distinct deformation crystallographic systems as shown in Table 1. Notably, Type-I.1 is the conjugate twinning mode of the commonly observed Type-II.1 twinning mode. In most SMAs, when one of a conjugate pair is prevalent, its conjugate forms with comparable frequency [61–64]. NiTi martensite, however, displays anomalous behavior: the non-conjugate Type-I.2 twinning mode often nucleates alongside Type-II.1 than expected. This crystallographic relationship is tabulated in Table 2. Conjugate twinning modes, such as Type-I.1 and Type-II.1, are characterized by equal twinning shear magnitudes (s) and an interchange of their primary and secondary invariant planes (K_1, K_2) and twinning shear directions (η_1, η_2), as illustrated in Fig. 1. One can show that they map onto each other by simple rotation operation. When the shear directions map due to a simple rotation, the twin planes must also match under the same rotation. In contrast, Type-I.2 remains non-conjugate to Type-II.1 yet nevertheless co-forms with it at unusually high frequency, which points to other factors such as the twin fault energies playing a considerable role. This aspect is the focus of the current work.

It is worth emphasizing that the Type-I.1 and Type-I.2 twinning modes considered in this study are the conjugate and non-conjugate to the Type-II.1 twinning mode in all the B19'-monoclinic systems. The Type-I TBs are observed in the B19' phase, which is generally known unit-cell. The atomic-site at the lattice point of the unit-cell is termed a lattice-site and the remaining atomic-positions within the cell are defined as the motif points. These atom positions should be determined accurately prior to modeling twin interface. Also, to accurately model the twin interface in atomistic simulations, the irrational twinning direction must be defined in a manner that remains compatible with periodic boundary conditions. Once this twinning direction is clarified, the atomistic structure needs to be determined in order to compute the TB energy. To determine the atomic-structure on the interface, a key unknown to be computed is known as the "lattice-offset" which specifies the relative positioning of the twin lattice with respect to the matrix. Although there were several interatomic potentials of NiTi in classical molecular dynamics (MD) that can capture mechanical properties [31,32,65–67] and have merits, these do not always guarantee a reliable reproduction of NiTi for such as TB energy [60] and superelasticity [68]. Given this aspect, our approach is to determine lattice-offsets more accurately using Density Functional Theory (DFT) calculations as proposed in this study. Furthermore, the analysis of the new Type-I systems reveals an important distinction between the $\{011\}$ and $\left\{11\bar{1}\right\}$ shear planes for the first time in this study to the best of the authors' knowledge. The simulation methods and results of the study are elaborated in Section 2 and discussed in Section 3, and the conclusions of the study are presented in Section 4.

Table 2
Twinning elements of representative twinning modes in NiTi martensites.

Twinning Mode	K_1	η_1	K_2	η_2	s	Comments
$\left\{11\bar{1}\right\}$ Type-I.2	$\left(\bar{1}11\right)$	[0.5404 0.4596 1]	(0.2470 0.5061 1)	$\left[\bar{2}11\right]$	0.30961	Non-conjugate (observed)
	$\left(\bar{1}11\right)$	$\left[0.5404\ \overline{0.4596}\ 1\right]$	$\left(0.2470\ \overline{0.5061}\ 1\right)$	$\left[\bar{2}11\right]$		
$\{011\}$ Type-I.1	(011)	$\left[1.57271\ 1\ \bar{1}\right]$	$\left[0.72053\ 1\ \bar{1}\right]$	[011]	0.28040	Conjugate (rarely observed)
	$\left(01\bar{1}\right)$	$\left[\overline{1.57271}\ 1\ 1\right]$	$\left[\overline{0.72053}\ 1\ 1\right]$	$\left[01\bar{1}\right]$		
$\langle 011\rangle$ Type-II.1	$\left[0.72053\ 1\ \bar{1}\right]$	[011]	(011)	$\left[1.57271\ 1\ \bar{1}\right]$	0.28040	Conjugate (observed)
	$\left[\overline{0.72053}\ 1\ 1\right]$	$\left[01\bar{1}\right]$	$\left(01\bar{1}\right)$	$\left[\overline{1.57271}\ 1\ 1\right]$		

2. Methodology and results

2.1. Atomistic simulations

For atomistic modeling of Type-1 twinning modes in NiTi martensite, we implement density functional theory (DFT) calculation [69] throughout the entire study. The DFT calculations are implemented within the projected-augmented-waves (PAW) [70] approach via Perdew-Burke-Ernzerhof (PBE) [71] exchange-correlation potentials. The PAW-PBE pseudopotentials for Ti and Ni are employed with the following valence electron configurations Ti ($3s^2$, $3p^6$, $3d^3$, $4s^1$) and Ni ($3p^6$, $3d^9$, $4s^1$), respectively. Initial k-mesh and plane-wave energy cutoff for NiTi unit-cell are optimized by Self-Consistent-Field (SCF) electronic minimization (See Supplementary materials **Fig. S1**). The Monkhorst-pack automatic k-mesh is applied for SCF, ionic and cell relaxations in allowing full distortions. A 450 eV plane-wave energy cutoff is used for all the calculations. The tolerance criteria for energy and force are allowed within 1 meV and 5 meV/Å, respectively. All DFT calculations, from the lattice parameters to twin interfaces and motions, were consistently performed using the parameters above.

To benchmark the accuracies of conventional empirical interatomic potentials, we conducted additional molecular dynamics (MD) simulations using three potentials for NiTi in the literature. These are developed by Ren-Sehitoglu (RS) [31], Ko-Grabowski-Neugebauer (KGN) [32], and Tang-Wang-Li (TWL) et al. [33]. For each potential, the lattice parameters and atomic positions were either adopted from the literature or determined in this study. For the KGN and TWL potentials in B19' phase, we took lattice parameters from the original literature and obtained atomic positions by energy minimization of the primitive unit cell after random perturbation of the lattice and motif`s positions [68]. All structural optimizations, from the lattice parameter to twin interfaces, were performed using the conjugate-gradient algorithm via the Large-scale Atomic/Molecular Massively Parallel Simulator (LAMMPS) [72]. The atomic configuration viewer Ovito [73] was used to reveal the unit-cell and twin interfaces. Crystal Maker is used to simulate diffraction patterns for the unit-cell and lattice-offsets.

2.2. Lattice parameters and atom positions

Accurate determination of lattice parameters and atomic positions is essential prior to modeling the twin interface, as these structural inputs critically influence subsequent calculations of twin boundary energies and migration behavior [68]. Accordingly, we begin with accurate determination of these values. We use a general volumetric-energy method in the determination of the lattice constants of NiTi. We first determine the lattice constants of B2 austenite phase using 9 × 9 × 9 k-mesh. B19 and B19' unit cell are then subjected to the same k-mesh through SCF, ionic and cell relaxation. Details of calculations in lattice constants are referred to the previous works [74,75]. With the optimized B2 unit-cell (2-atom), we constructed a tetragonal B19 cell (4-atom) and systematically varied its lattice parameters (*a, b*, and *c*) to determine the orthorhombic B19 cell. We illustrate this procedure in detail in **Fig. S2** in the Supplementary material. Fig. 2**a** plots the total energy (per atom) as a function of the lattice parameters (normalized by a = 2.934 Å), with the energy minimum indicated by the yellow marker. Then, the lattice-motifs (2-Ti, 2-Ni atoms) of the B19 cell were fully relaxed including both cell and atom positions. Using this cell, we then scanned the monoclinic angle between 90° and 100° (Fig. 2**b**) to locate the energy-minimum, followed by a full relaxation including cell to refine the atom positions. Intermediate cell parameters are provided in Supplementary material **Table S1**, while the final lattice parameters for B2, B19, and B19' cells are listed in Table 3 and compared with previous theoretical and experimental values [31–33,76,77].

The accuracy of atom positions not only affects the energy landscape of twin interfaces but can also be directly assessed for experimental fidelity. We simulated electron diffraction patterns for the B19' martensite phase using both accurate and inaccurate atom positions, as shown in Fig. 3, and compared these with experimental patterns. We also included the results of Ren-Sehitoglu (RS), Ko-Grabowski-Neugebauer (KGN), and Tang-Wang-Li et al. (TWL) interatomic potentials in MD for NiTi [31–33], with atom positions [68] for the same zone axis [011] (See **Fig. S3** for TWL result). The RS- and DFT-based atom positions in this study reproduce all expected diffraction peaks along the a- and $b+c$-axes. In the meanwhile, the KGN model fails to position certain motif atoms on the planes such as $(01\bar{1})$, $(\bar{1}1\bar{1})$, $(2\bar{1}1)$, and $(02\bar{2})$, resulting in missing or weaker peaks. The discrepancy demonstrates that the existing MD potentials with incorrect atom positions can lack physical fidelity for modeling NiTi martensite. In contrast, the DFT-based atom positions yield diffraction patterns in excellent agreement with experiment, as also summarized in Table 3. This comparison is not limited to one zone axis, as shown in **Fig. S4** for [110] zone axis in the Supplementary materials. In such zone axis, $(\bar{1}10)$ and (002) planes can be missed by the MD model.

2.3. Irrational twinning shear direction

In this section, we elaborate a procedure for constructing twin interface supercells tailored to atomistic simulations. Since the Type-I twin-

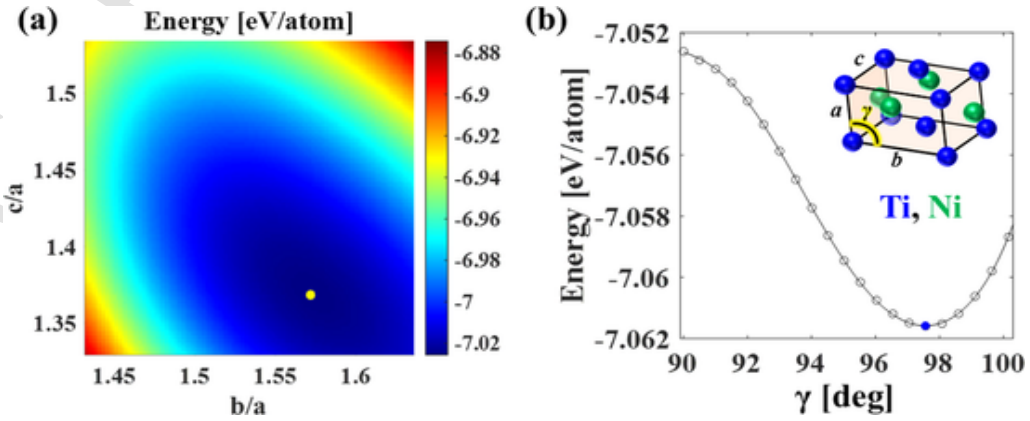

Fig. 2. Determination of lattice parameters of NiTi martensite; (a) Lattice parameters of orthorhombic B19 cell of NiTi, (b) Monoclinic angle of B19' martensite of NiTi. The minimum energy points are denoted as yellow and blue circles. Schematic of NiTi martensite unit-cell is shown in the inset (Ni: green, Ti: blue).

Table 3
Lattice parameters and atom positions of NiTi austenite (B2), hypothetical orthorhombic (B19), and martensite (B19'). Atom positions (motifs) are in fractional coordinates. Lattice Ti atom is set as origin, Ti_0: (0 0 0), and the relative positions of motif Ti (Ti_1) and Ni atoms (Ni_0, Ni_1) are tabulated.

	a [Å]	b [Å]	c [Å]	γ [°]	Ti_1	Ni_0	Ni_1
B2 (This study, DFT)	3.004	4.248	4.248	90	(0 0.5 0.5)	(0.5 0.5 0)	(0.5 0 0.5)
B2 (Expt[a].)	3.015	4.264	4.264	90	(0 0.5 0.5)	(0.5 0.5 0)	(0.5 0 0.5)
B2 (HAR[b], DFT)	3.009	4.255	4.255	90	(0 0.5 0.5)	(0.5 0.5 0)	(0.5 0 0.5)
B19 (This study, DFT)	2.889	4.581	4.123	90	(0 0.5474 0.5)	(0.5 0.4586 0)	(0.5 0.0888 0.5)
B19 (HAR[b], DFT)	2.859	4.582	4.078	90	(0 0.5620 0.5)	(0.5 0.4650 0)	(0.5 0.0097 0.5)
B19' (This study, DFT)	2.923	4.672	4.060	97.6	(0.1647 0.5626 0.5)	(0.6262 0.4556 0)	(0.5385 0.1065 0.5)
B19' (Expt[c].)	2.898	4.646	4.108	97.8	(0.1648 0.5672 0.5)	(0.6196 0.4588 0)	(0.5452 0.1084 0.5)
B19' (HAR[b], DFT)	2.929	4.686	4.048	97.8	(0.1756 0.5654 0.5)	(0.6347 0.4582 0)	(0.5409 0.1072 0.5)
B19' (RS[d], MD)	2.699	4.606	4.386	93.41	(0.341 0.697 0.5)	(0.665 0.491 0)	(0.677 0.207 0.5)
B19' (KGN[e], MD)	2.878	4.659	4.129	99.4	(0.295 0.779 0.5)	(0.476 0.522 0)	(0.819 0.257 0.5)
B19' (TWL[f], MD)	2.89	4.72	4.03	101.03	(0.209 0.576 0.5)	(0.653 0.460 0)	(0.555 0.116 0.5)

[a] Expt [76]., Huang-Ackland-Rabe (HAR).
[b] [77], Expt.
[c] [78], Ren-Sehitoglu (RS).
[d] [31], Ko-Grabowski-Neugebauer (KGN).
[e] [32], Tang-Wang-Li et al. (TWL).
[f] [33].

ning shear directions are defined by irrational crystallographic vectors, it is essential from a modeling standpoint to transform these into the rational vectors for compatibility with periodic boundary conditions. From classical twinning theory [34], it is well established that the twin variant is related to the matrix by an Invariant Plane Strain (IPS) and the invariant plane is the plane of twinning. The IPS is given by the deformation gradient of the form:

$$F_{tw} = \left(I + s\left(\hat{\eta}_1 \otimes \hat{n}_K\right)\right) \tag{1}$$

where s is the classical twinning shear (listed in Table 2), the unit vector along the direction of irrational twinning $\hat{\eta}_1$ and the unit normal $\hat{n}_{K_1}$ of the twinning plane (refer to Fig. 4**a**). In the coordinate system $\hat{\eta}_1 - \hat{\nu} - \hat{n}_{K_1}$ defined on the irrational twinning shear direction, the deformation gradient is given by:

$$\left[F_{tw}\right]_K = \begin{pmatrix} 1 & 0 & s \\ 0 & 1 & 0 \\ 0 & 0 & 1 \end{pmatrix} \tag{2}$$

Consider the same deformation gradient resolved along a coordinate system attached to the rational terrace plane, $\hat{\eta}_T - \hat{\nu}_T - \hat{n}_{K_1}$ as illustrated in Fig. 4**b** In this coordinate system, the deformation gradient is obtained from a rotational transformation, Q, given by the following equations:

$$\left[F_{tw}\right]_T = [Q]^T \left[F_{tw}\right]_K [Q]$$
$$[Q] = \begin{pmatrix} \cos\theta & \sin\theta & 0 \\ -\sin\theta & \cos\theta & 0 \\ 0 & 0 & 1 \end{pmatrix} \tag{3}$$
$$\left[F_{tw}\right]_T = \begin{pmatrix} 1 & 0 & s_1 \\ 0 & 1 & s_2 \\ 0 & 0 & 1 \end{pmatrix}$$

where θ is the angle of deviation between the irrational twinning direction η_1 and the rational twinning direction η_T (see Fig. 4 and Table 3). Note that the components of the deformation gradient F_{tw} resolved in the rational coordinate system (described by $\left[F_{tw}\right]_T$ in Eq. (3)) directly yields two rational twinning shears (s_1, s_2). The secondary rational shear s_2 is the shear required to twin on the rational coordinate system. From Eq. (2) and (3), the rational twinning shears (s_1, s_2) can be determined as functions of θ and s as follows:

$$s_1 = s\cos\theta; s_2 = s\sin\theta \tag{4}$$

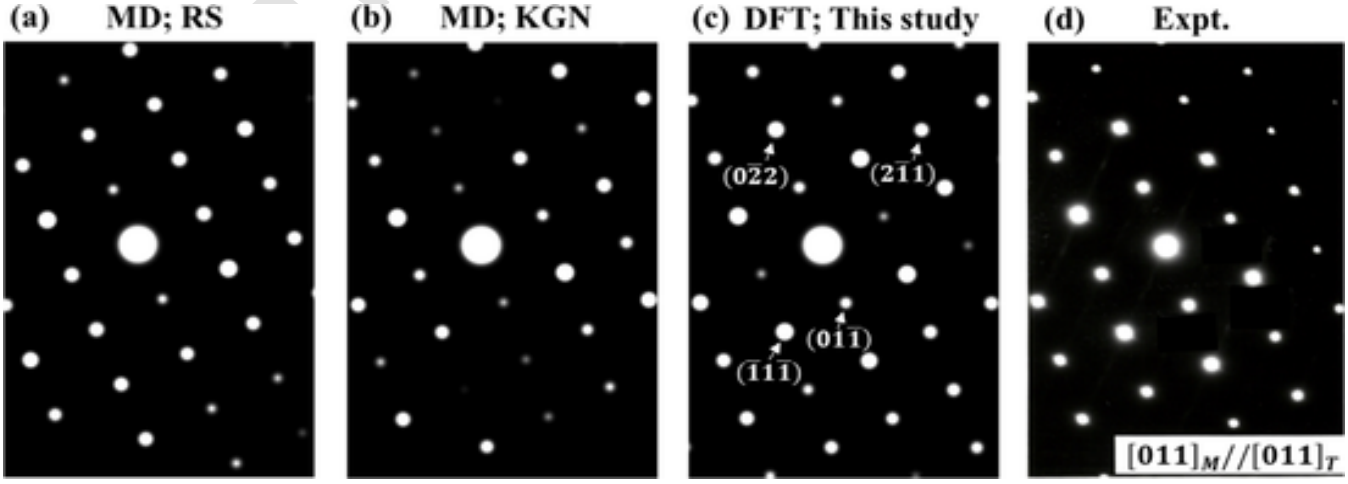

Fig. 3. Comparison of electron diffraction patterns with different lattice parameters and atom positions. Simulated patterns based on the optimized atom positions with (a) MD potential developed by RS, (b) KGN, (c) DFT in this study, and the pattern (d) observed in experiment [46]. All diffraction patterns are on zone axis [011].

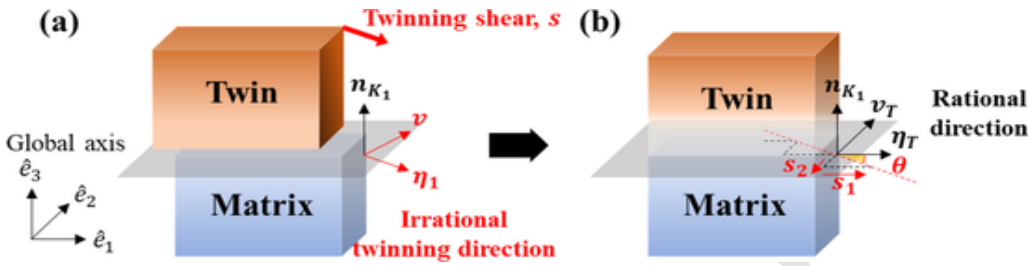

Fig. 4. Deformation gradient relating the twin to the matrix described in two frames of reference (a) the conventional coordinate system based on direction of irrational twinning shear η_1, normal to the twinning plane ${}^{n}K_1$, and a third orthonormal vector v of Type-I twinning modes. (b) In the rational coordinate system described by the rational twinning shear direction η_T, plane-normal ${}^{n}K_1$, and their third orthonormal vector ${}^{v}T$, the deformation-gradient reveals two rational twinning shears (s_1, s_2); the angle between the rational and irrational twinning directions, θ, is also illustrated.

Table 3 lists all the rational twinning shears for the Type-I of NiTi martensite considered, note that they are all not equal to the respective classical twinning shears. The twin structures with these rational twinning systems can accurately capture the TB energy within 1 mJ/m^2 error range. Table 4

With the correct atom positions and rational coordinate systems suitable for the simulations, the TB structure can now be constructed. First, a periodic simulation cell suitable for the TB structure must be defined. Since the DFT calculations are expensive and scale quickly with the number of atoms, the least number of atoms is strongly recommended in the structure. Owing to the non-cubic structure of the martensite, the simulation cell is found to be triclinic, illustrated in Fig. 5**a** (an example of {011} Type-I.1). The bounding box vectors $\vec{L}_1 - \vec{L}_2 - \vec{L}_3$ are defined, such as the vector $\vec{L}_1 = \left[21\bar{1}\right]$, $\vec{L}_2 = \left[1\bar{1}1\right]$, and $\vec{L}_3 = 4[011]_M$ in the martensitic matrix variant index, respectively. The determination of these vector components is given in the Supplementary materials. A total of 16 $K_1 = (011)$ planes are simulated with $N = 8$ planes corresponding to the twin variant, remaining 8 to the matrix variant, and with each plane containing 6 atoms within two-periodicity (shown in Fig. 5**b**). To incorporate N twin planes, the vector $\vec{L}_3$ must be incremented by $Ns_1d_{(011)}$ along $\vec{L}_1$ and by $Ns_2d_{(011)}$ along $\vec{L}_2$ direction, respectively, where $d_{(011)}$ is the interplanar spacing, accounting for the rational twinning shears in the system (Fig. 5**b-c**). This is necessary as without these shears correctly, the periodicity across the top and bottom boundaries of the simulation cell would be broken precluding an accurate simulation of the twinned structure.

Table 4
Irrational and transformed-rational twinning shears of Type-I.

Twinning mode	Twinning shear, s	Twinning direction, η_1	Rational direction, η_T	Angle of deviation, θ	Rational twinning shears (s_1, s_2)
{011} Type-I.1	0.28040	$\left[1.5727\ 1\ \bar{1}\right]$	$\left[2\ 1\ \bar{1}\right]$	6.13°	(0.2788, 0.0299)
$\left\{11\bar{1}\right\}$ Type-I.2	0.30961	[0.5404 0.4596 1]	[1 1 2]	2.22°	(0.3094, 0.0120)

2.4. Lattice offset

Here, the determination of "lattice-offset" is given for the Type-I TB interfaces. As shown in the previous section, the crystallography of twinning shear direction in the Type-I is not actually rational. Specifically, the relative position of the twin onto matrix variant is not clear if two variants are commensurate with each other. This relative position is otherwise termed as the "lattice-offset", defined and determined for the TBs considered as follows. Two reference origin points O_{tw} and O_M are chosen on the lattice-sites of two crystallographic planes P_{tw} and P_M, shown in Fig. 6**a**. The lattice and motif sites were referred to Section 2.2. We established the procedure for {011} Type-I.1 as an example here, and the case of $\left\{11\bar{1}\right\}$ Type-I.2 is given in Fig. A1 in the

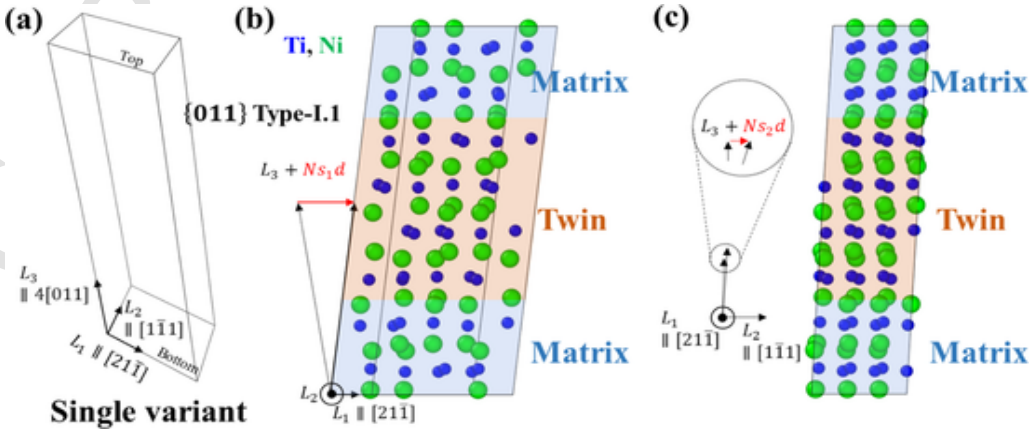

Fig. 5. Construction of atomistic simulation cell for Type-I interfaces ({011} Type-I.1 for example): (a) Triclinic simulation cell with lattice vectors $L_1 - L_2 - L_3$ are defined. Twinned structure constructed within simulation cell in the view of (b) L_2 and (c) L_1. The longitudinal vector L_3 is corrected with the applied rational twinning shears (s_1, s_2), and the number of twin planes N (with interplanar spacing d); there are 6 atoms per {011} plane with two-periodicity.

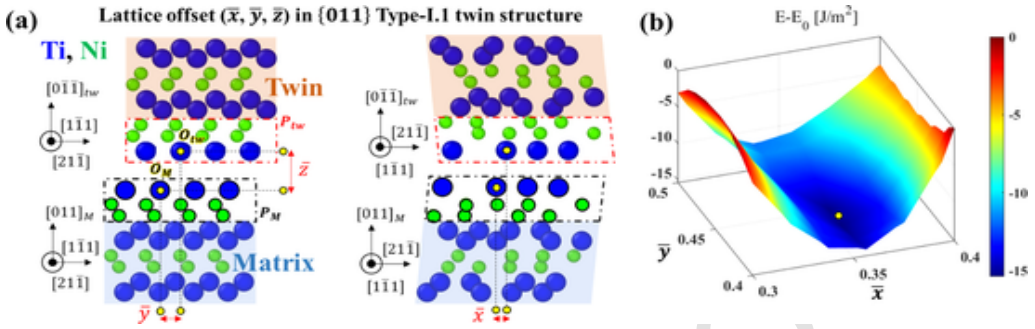

Fig. 6. Determination of lattice-offset for construction of twin boundary structure ({011} Type-I.1 for example): (a) Defining the normalized lattice-offsets ($\bar{x}$, $\bar{y}$, $\bar{z}$); (b) Energy-minimizing offset is determined from DFT-SCF simulations (E is the potential energy at a general offset ($\bar{x}$, $\bar{y}$) and E_0 is the energy at offset (0, 0), but $\bar{z} = 0.063$).

Appendix A. The plane P_{tw} lies on the twin variant and P_M is a virtual crystallographic plane that were to exist if the matrix variant was presumed to extend by one more plane into the twin. The triad vector (x, y, z) describing the relative position of O_{tw} with respect to O_M defines the lattice-offset vector that needs to be determined. Given the periodicity of the lattice, the vector can be defined in a normalized form given by:

$$\bar{x} = \frac{x}{\left|\left[2\bar{1}\bar{1}\right]\right|}; \bar{y} = \frac{y}{\left|\left[1\bar{1}1\right]\right|}; \bar{z} = \frac{z}{d_{(011)}} \quad (5)$$

where $d_{(011)}$ is the interplanar spacing of the (011) planes. The component $\bar{z}$ can be determined based on the conservation of crystal volume during twinning. It requires the interplanar spacing to be preserved as one plane moves from the matrix to the twin variant, which results in $\bar{z} = 0.063$.

The magnitudes of $(\bar{x}, \bar{y})$ are not known apriori, which require atomistic simulation. At incremental magnitudes of both $(\bar{x}, \bar{y})$ between 0 and 1, an SCF calculation is performed to determine the potential energy of the atomic-structure at that offset. We use $9 \times 9 \times 1$ k-mesh for the subsequent supercells including SCF, ionic and cell relaxation to hinder redundant fault outside the periodic boundary. The magnitudes of $(\bar{x}, \bar{y})$ that yield the lowest energy are determined as shown in Fig. 6**b**, indicated by the yellow marker. The relative changes in the TB potential energy are plotted with respect to the energy at zero-offset i.e. at $(\bar{x}, \bar{y}) = (0, 0)$. The optimum lattice-offsets were found at (0.358, 0.441). The finding of non-trivial lattice-offsets is consistent with prior results in Type-II.1 TB structures of SMAs as reported in the previous works [15,74]. An incorrect lattice-offset could give a significantly erroneous TB energy (~1100 mJ/m^2) as shown in **Fig. S5** in the Supplementary materials. The optimum lattice-offset now unambiguously defines the relative position of the twin variant with respect to the matrix. The resulting Type-I TB structures are then fully relaxed including cell, and the total energies of relaxed TB structures are used to obtain the planar TB energies, E_{TB}. Prior to the discussion of these results in the next Section 2.5, we additionally analyze the diffraction patterns of lattice-offsets below.

Fig. 7**a-b** show simulated diffraction patterns for the TB interfaces with all triad lattice-offsets $(\bar{x}, \bar{y}, \bar{z})$ to (0, 0, 0) and with the optimum lattice-offsets based on the crystallography and energy-minimization, respectively. When compared to the experimental diffraction pattern (Fig. 7**c**), the simulated pattern employing the optimized lattice-offsets reproduces the observed peak positions and intensities with high fidelity. In contrast, neglecting all offsets produces pronounced disagreements, including the appearance of forbidden reflections and attenuated peak intensities. Specifically, omitting the $\bar{z}$-offset gives rise to unexpected peaks along the normal direction of twin-plane (red arrows).

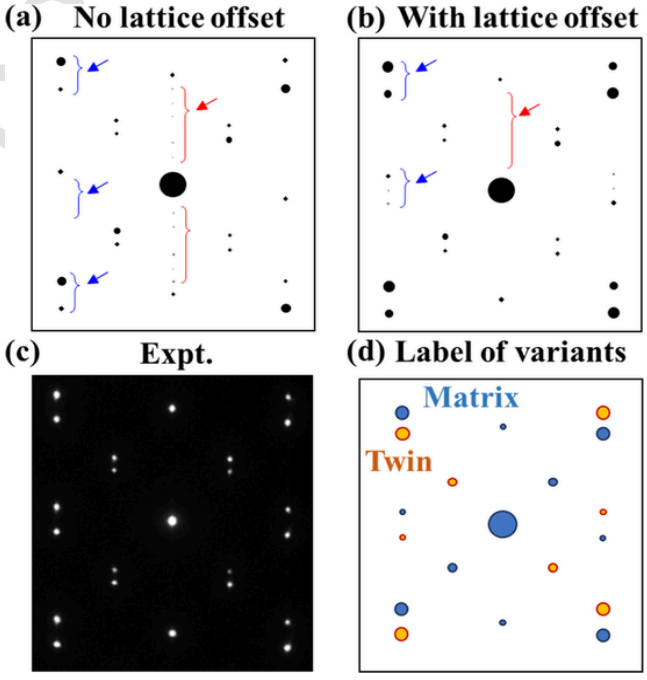

Fig. 7. Comparison of electron diffraction patterns with lattice offset ({011} Type-I.1 for example): Simulated patterns based on (a) zero-offset, (b) the optimized lattice-offset. Arrows indicate the region of interest that shows significant differences; see the text. (c) The pattern observed in experiment. All diffraction patterns are on zone axis [100]. (d) Label of variants (matrix, twin) in diffraction patterns.

These are the artifacts of interplanar spacing mismatch on the (011) planes that would not occur under volume-conserving shear and are absent in the experimental pattern. Likewise, the zero-offsets in $(\bar{x}, \bar{y})$ weakens both matrix- and twin-variant peak intensities (blue arrows), indicating that the two variants (see Fig. 7**d**) do not properly commensurate at the interface. Thus, only by incorporating the full set of optimum lattice-offsets can one accurately capture both the peak positions and relative intensities observed experimentally. The results of $\{11\bar{1}\}$ Type-I twin example are shown in the Supplementary materials. This direct comparison of lattice-offset to the experiment is first time in the literature to the best knowledge.

2.5. Twin boundary

In this section, we compare the Type-I twin boundary (TB) energies E_{TB} calculated based on the optimum lattice-offsets in the previous section. E_{TB} is defined as follow,

$$E_{TB} = \frac{E - E_0}{2A} \tag{6}$$

where $2A$ is 2 times of box area (sandwich) and $E_0 = NE_{B19'}$ is martensite matrix energy (a single variant) for N and $E_{B19'}$ which are martensite energy per atom and its total number of atoms. Fig. 8 plots the DFT-based E_{TB} alongside those obtained from several empirical MD-based interatomic potentials. These are also tabulated in Table 5 for the martensitic unit-cell atomic-positions, optimum lattice-offsets, and E_{TB} corresponding to potentials. In Fig. 8**a**, the earlier investigation of the Type-I E_{TB} reported nearly identical energies 230 mJ/m^2 and 235 mJ/m^2 for Type-I.1 and Type-I.2 [60], failing to account for their differing observation frequencies. By contrast, an accurate determination of lattice-motif positions and lattice-offsets reveals a clear energy separation, such that 141 mJ/m^2 and 42 mJ/m^2. The twinnability of a given mode is dictated by the complete twinning-energy landscape, i.e., the GPFE, defining the stable twin-boundary energy, E_{TB}, and the twin-migration energy, γ_{TM}, influencing mobility. In this study, we note that the GPFE (Section 2.6) of the $\left\{11\bar{1}\right\}$ Type-I.2 twin, in its entirety, is lower than that of the $\{011\}$ Type-I.1 twin, with a lower TB energy and lower twin-migration energy, correlating directly with its higher experimental prevalence. We further include a comparison of $\langle 011\rangle$ Type-II.1 E_{TB}, and the MD-based results are systematically overestimated and less accurate. On this aspect, we also summarized an extensive comparison of Type-I E_{TB} across various MD potentials in Fig. 8**b** and Table 5. Each case employs its own optimized lattice parameters (Table 3), atomic positions, and lattice-offsets. The energy landscapes on lattice-offsets for different MD potentials are given in **Fig. S6–8** the Supplementary material. Among the MD potentials considered in this study, the RS model most faithfully reproduces the pronounced energy hierarchy between two Type-I twinning modes, followed by the KGN and TWL models. Notably, even within a single potential (e.g., KGN), the predicted twinning mode ranking reverses if accurate lattice-offsets are omitted. These results highlight that, the choice of empirical potential and the determination of accurate atom positions and lattice-offsets, are both critical for capturing physically meaningful TB energetics as well as for any large-scale simulation in which twinning plays a central role.

We next analyze how each Type-I twin interface configures an arrangement in atomistic scale with the corresponding TB energy. We also compare, as thoroughly as possible, the twin interfaces based on experimental observations and DFT simulations. Type-I twinning mode interfaces have been directly imaged by high resolution scanning transmission electron microscopy (HRSTEM). Experimental procedures can be found in the Appendix B. Fig. 9 presents the non-conjugate $\left\{11\bar{1}\right\}$ Type-I.2 twinning mode interface alongside the corresponding (part of) atomistic configuration from the DFT simulation. A full-size of DFT configuration is in Fig. A2 in the Appendix A. In Fig. 9**a**, we display the representative twinning mode hierarchy of $\left\{11\bar{1}\right\}$ Type-I.2 and $\langle 011\rangle$ Type-II.1 accommodation. Fig. 9**b** provides a magnified view of the Type-I.2 region as a focus in this study. Fig. 9**c** shows the intensity profile along the TB plane, where Ni atoms appear brighter than Ti due to their higher atomic number (or mass). The alternating Ti and Ni predicted by DFT (Fig. 9**d**) is clearly manifest in both simulation and experiment. Although complete atomic discrimination is limited when atoms overlap, the experimentally observed $\left[\bar{1}1\bar{1}\right]$ plane line in both matrix and twin variants matches the atomistic model with remarkable accuracy. To the best authors' knowledge, this is the first study to combine accurate TB energy calculations, atomic-species contrast, and a strong structural correspondence with HRSTEM data.

Similarly, we examined the rarely-observed conjugate $\{011\}$ Type-I.1 twinning mode interface. Fig. 10 presents, in a manner analogous to $\left\{11\bar{1}\right\}$ Type-I.2, the intensity-based differentiation of Ni and Ti atoms and the corresponding atomistic configurations. In Fig. 10**a**, the HRSTEM image of the Type-I.1 twin interface is shown, and the intensity profile extracted along the yellow dashed line (red arrow direction) is plotted in Fig. 10**b**, revealing an alternating Ni and Ti sequence. Fig. 10**c-d** depict the zigzag projection of these two species along the direction [001] in the zone axis [100]. A full-size of DFT configuration is in **Fig. S5** in the Supplementary materials. Along the TB plane, Ti atoms occupy the interface and form a flat profile, as previously reported [79]. Unlike $\left\{11\bar{1}\right\}$ Type-I.2, $\{011\}$ Type-I.1 twin interface does not exhibit overlapping atoms, although a difference arising not merely from the projecting zone axis but from the distinct atomic densities of each

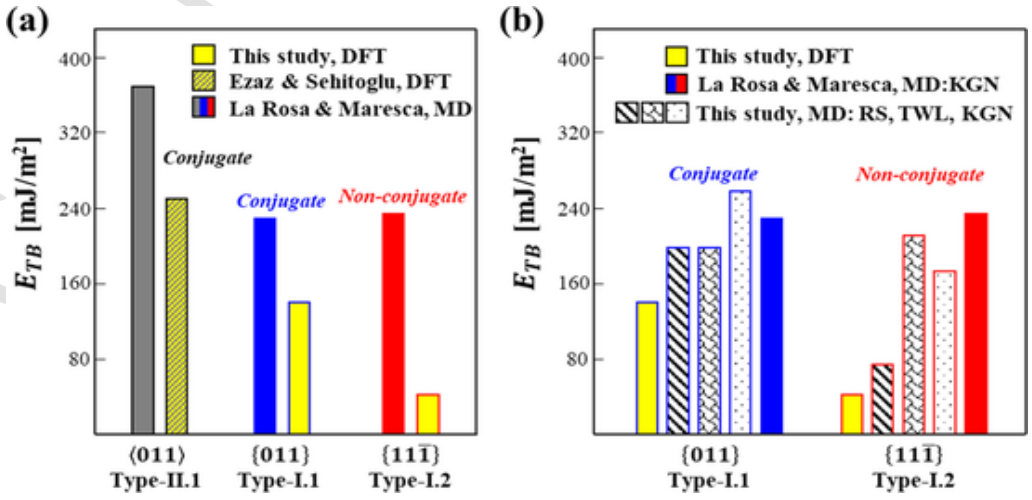

Fig. 8. (a) Twin boundary (TB) energies, E_{TB}, of representative twinning modes in NiTi martensite. (b) E_{TB} of Type-I based on DFT and empirical potentials (MD) in this study. The results are compared with an earlier work based on MD potential (KGN).

Table 5
TB energies of Type-I twinning modes based on different potentials.

Twinning mode	Lattice-Motif atomic positions	Lattice offset triad ($\bar{x}$, $\bar{y}$, $\bar{z}$)	TB energy E_{TB} [mJ/m^2]	Ref.
{011} Type-I.1 (*Conjugate*)	Ti (0, 0, 0), (0.165, 0.563, 0.5) Ni (0.626, 0.456, 0), (0.538, 0.106, 0.5)	(0.358, 0.441, 0.063)	141	This study, DFT
	Ti (0, 0, 0), (0.341, 0.697, 0.5) Ni (0.665, 0.491, 0), (0.677, 0.207, 0.5)	(0.573, 0.131, 0.197)	196	This study, MD (RS potential)
	Ti (0, 0, 0), (0.209, 0.576, 0.5) Ni (0.653, 0.460, 0), (0.555, 0.116, 0.5)	(0.392, 0.863, 0.076)	195	This study, MD (TWL potential)
	Ti (0, 0, 0), (0.295, 0.779, 0.5) Ni (0.476, 0.522, 0), (0.819, 0.257, 0.5)	(0.000, 0.594, 0.279)	256	This study, MD (KGN potential)
	Ti (0, 0, 0), (0.295, 0.779, 0.5) Ni (0.476, 0.522, 0), (0.819, 0.257, 0.5)	–	230	La Rosa & Maresca, MD (KGN potential)
$\{11\bar{1}\}$ Type-I.2 (*Non-conjugate*)	Ti (0, 0, 0), (0.165, 0.563, 0.5) Ni (0.626, 0.456, 0), (0.538, 0.106, 0.5)	(0.698, 0.703, 0.103)	42	This study, DFT
	Ti (0, 0, 0), (0.341, 0.697, 0.5) Ni (0.665, 0.491, 0), (0.677, 0.207, 0.5)	(0.095, 0.320, 0.144)	75	This study, MD (RS potential)
	Ti (0, 0, 0), (0.209, 0.576, 0.5) Ni (0.653, 0.460, 0), (0.555, 0.116, 0.5)	(0.425, 0.119, 0.133)	210	This study, MD (TWL potential)
	Ti (0, 0, 0), (0.295, 0.779, 0.5) Ni (0.476, 0.522, 0), (0.819, 0.257, 0.5)	(0.299, 0.296, 0.016)	174	This study, MD (KGN potential)
	Ti (0, 0, 0), (0.295, 0.779, 0.5) Ni (0.476, 0.522, 0), (0.819, 0.257, 0.5)	–	235	La Rosa & Maresca, MD (KGN potential)

plane. The atomic densities for {011} Type-I.1 and $\{11\bar{1}\}$ Type-I.2 are 0.111 Å^{-2} and 0.160 Å^{-2} (atoms per unit area), respectively; the higher planar density corresponds to the lower TB energy (141 mJ/m^2 and 42 mJ/m^2), in agreement with our computed trends (see Fig. C1 in the Appendix C).

2.6. Twin migration and nucleation

In this section, we investigate twin migration and nucleation on the interface. Both processes are governed by coupled twinning shear-shuffle, where the "shuffle" denotes additional atomic displacements beyond the simple shear-magnitude. To characterize these contributions, we begin with the energetically optimized TB structures obtained in the previous section, which incorporate the optimal lattice-offsets. As illustrated in Fig. 11**a** (an example of {011} Type-I.1), a nascent twin layer is introduced one plane above or below the previous interface, and the system is fully relaxed including cell to obtain the new equilibrium energy. Subtracting the shear displacement from the total atomic displacements measured relative to the original interface yields the atomic-shuffle vectors, as schematized in Fig. 11**b** The shuffle amplitude decays sharply with distance from the interface, so only the first crossing of the twin plane is shown. Upon twinning shear, Ti atoms move predominantly along the plane-normal direction, whereas Ni atoms displace additionally along the irrational twinning shear direction. The net sum of all atomic shuffles is zero, consistent with the previous studies [14,15,80,81]. Since atomic shuffle are not known apriori, its explicit calculation is essential for the subsequent analysis of nucleation energetics.

The shear–shuffle displacement for each Type-I twinning mode is now applied to a clean single variant (matrix) and we compute the twin nucleation–migration energetics. The complete energy profile, the generalized planar fault energy (GPFE) curve, was generated by incrementally shearing and shuffling the atoms plane-by-plane and recording the total energy (E) at each step,

$$\gamma = \frac{E - E_0}{A} \tag{7}$$

Except at the intrinsic twin stacking-fault point (γ_{tsf}, i.e., $2E_{TB}$), all atoms were constrained along the shear direction to prevent relaxation back to the unsheared state; only those atoms designated for shuffle in shear direction were permitted full relaxation including cell. Fig. 12**a** shows the full GPFE curves for {011} Type-I.1 and $\{11\bar{1}\}$ Type-I.2, demonstrating that non-conjugate Type-I.2 possesses both a lower nucleation energy (unstable twinning energy barrier γ_{ut}) and E_{TB}. Fig. 12**b** highlights the migration segment of the GPFE, with raw data points overlaid. Type-I.2 also exhibits a smaller twin migration energy barrier, γ_{TM}, than Type-I.1, and the combination of lower nucleation, migration, and TB energies quantitatively account for the higher observed frequency of non-conjugate Type-I.2. All calculated values for the Type-I twinning modes are tabulated in Table 6, also with conjugate ⟨011⟩ Type-II.1 [17]. We note that the simulations in this study isolated each single Type-I twinning mode to investigate a hierarchy of individuals; the interaction effects of coexisting twins (e.g., Type-I with Type-II or Compound) warrant future study.

3. Discussion of results

Research on transformation and twinning in NiTi alloys has continued for >50 years, emphasizing both scientific understanding and engineering applications. Many questions about elastic moduli, transformation strains, dislocation slip, and crystal lattices have been addressed through previous work [82–84]. The martensite is internally twinned to accommodate the transformation strains and reduce plastic flow via dislocation movement. The growth of martensite due to changes in stress and temperature depends on the mobility of twin interfaces. In this paper, we introduce a methodology to describe the energetics of twin interfaces. We use advanced experimental and theoretical tools to understand why the $\{11\bar{1}\}$ Type-I twin boundary (TB) is favored over the {011} Type-I boundary. The experiments are at high resolution scanning transmission electron microscopy (HRSTEM) precisely pinpointing

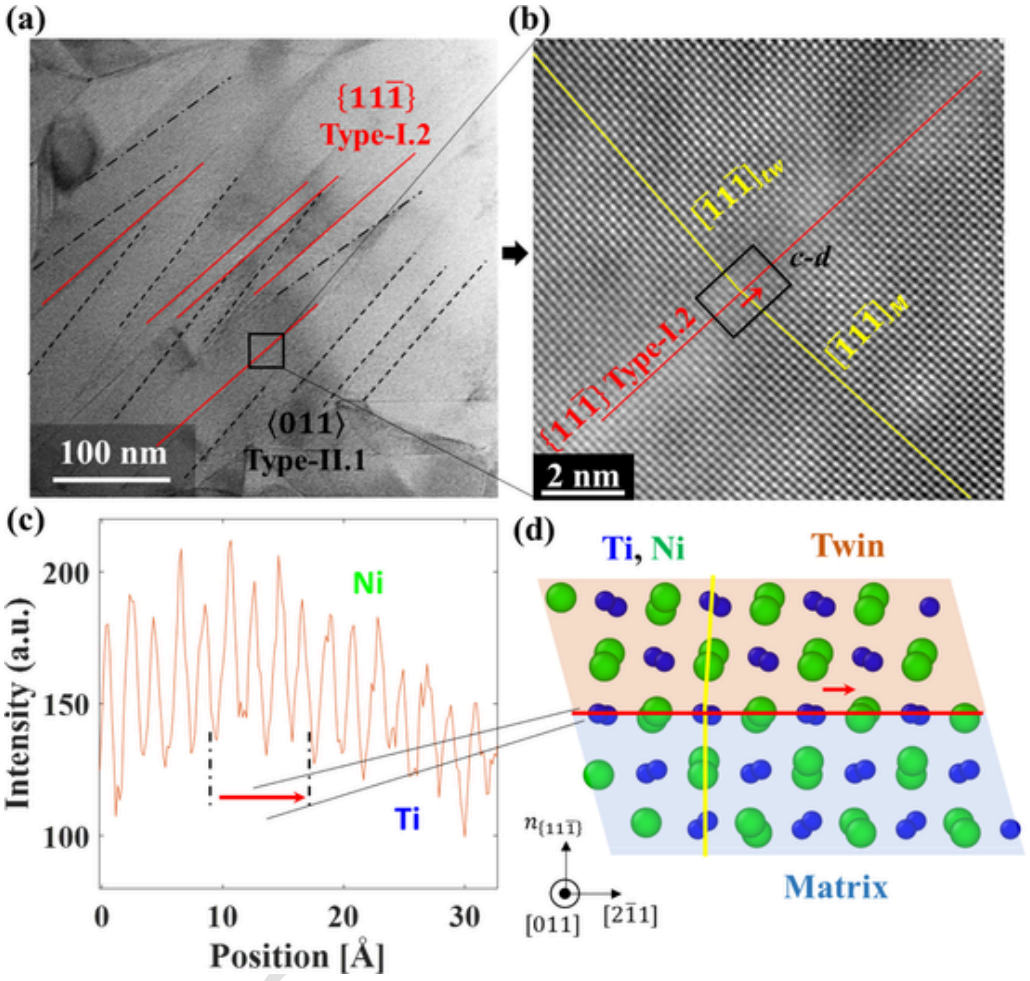

Fig. 9. (a) Bright field scanning transmission electron microscopy (BF-STEM) images of twinning modes ($\left\{11\bar{1}\right\}$ Type-I.2 and ⟨011⟩ Type-II.1). (b) $\left\{11\bar{1}\right\}$ Type-I.2twin interface via high-angle annular dark field (HAADF)-STEM. (c) Recognition of atomic species based on intensity along the twin plane. (d) $\left\{11\bar{1}\right\}$ Type-I.2 twin interface via DFT simulation. Zone axis is along $[01\bar{1}]$ for all images.

the corrugations and the accompanying electron diffraction. The theory is based on establishing the minimum energy configurations and ab-initio calculations. We systematically evaluate various TB structure proposals by others that document energetics based on existing molecular dynamics (MD) potentials, which have significant limitations. We avoid previous pitfalls by first establishing the interface and then evaluating the energetics of twin growth.

Twinning in NiTi martensites during phase transformation is recognized as lattice-invariant shear, which accommodates the large transformation strains by minimizing the overall energy [3,85]. In reversible transformations, twinning readily occurs during cooling in the absence of external stress (named shape memory), as well as under reversible deformation under loading and unloading (named superelasticity). The energy barriers associated with twinning in NiTi B19' martensites are considerably lower than those in the austenitic NiTi B2 phase and are also lower relative to many cubic crystals [11]. Therefore, twinning is an important deformation mode in martensite that imparts functionality to shape memory materials. This study is mainly concerned with transformation twins in martensite.

Previous MD potential-based calculations have predicted high energy barriers for $\left\{11\bar{1}\right\}$ Type-I twinning, a finding that contradicts experimental evidence highlighting its significance. In contrast, {011} Type-I twinning is seldom observed, yet a clear explanation for this phenomenon has not been provided. The present study undertakes a detailed examination of $\left\{11\bar{1}\right\}$ Type-I twinning, demonstrating that its energy barrier is substantially lower than that of {011} Type-I twinning. The results underscore the significance of utilizing ab-initio calculations that are not affected by the selection of specific MD potentials and the calculation of lattice-offsets at the interface.

We note that other twin elements such as compound {001} or {100} twins [29,54,55,78] are not a solution to the phenomenological theory of martensite transformation [85] as a lattice-invariant shear. However, if the transformation occurs through an intermediate R phase, then {001} is indeed a lattice-invariant shear [86]. These systems are summarized in early work, and the energy barriers have been established for {001}, {100}, and {201}. However, the Type-I TBs are difficult to determine at the atomic level because they are corrugated and experience significant lattice-offsets that are not known a priori. The current work addressed these issues.

The study highlights the limitations of MD potentials in assessing NiTi twinning, and mainly two issues are noted: (1) lattice offsets must be identified by analyzing the entire energy landscape because multiple close minima exist, and (2) MD potentials may not always find the correct lattice offsets, even when energy minimization is correctly per-

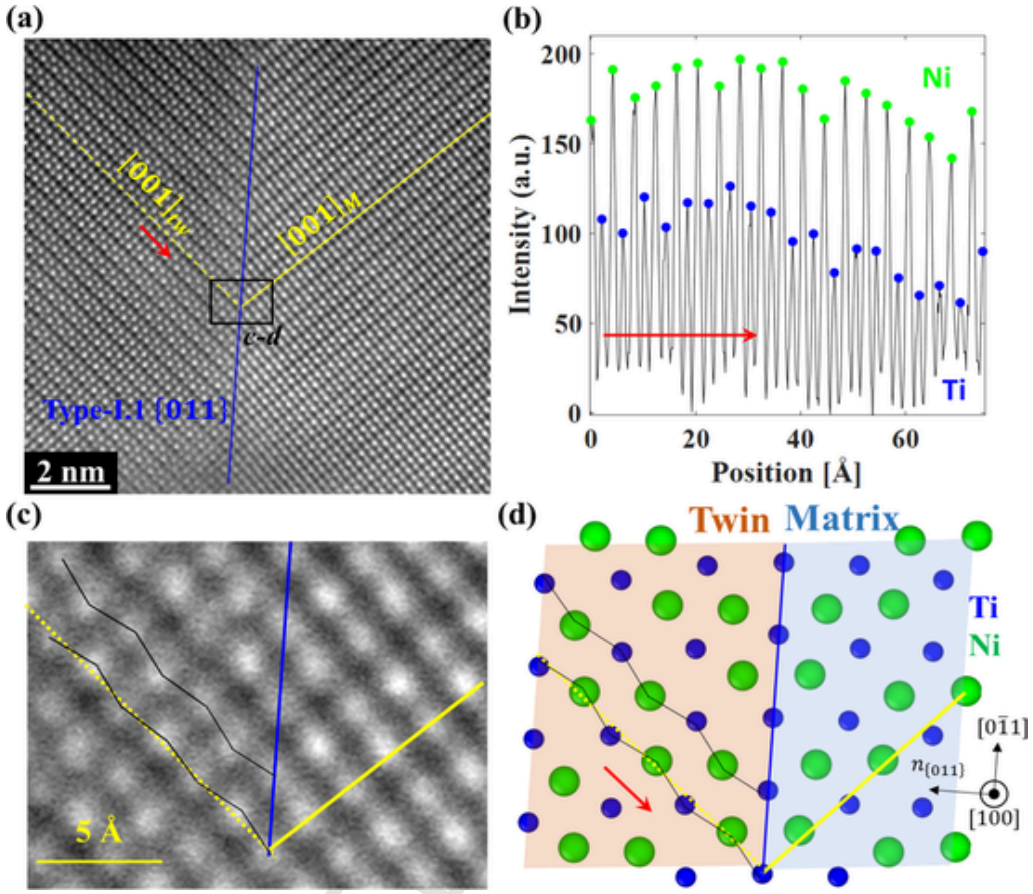

Fig. 10. (a) High resolution scanning transmission electron microscopy (HRSTEM) image of $\{011\}$ Type-I.1 twinning mode. (b) Recognition of atomic species based on intensity along $[001]$ line annotated by red arrow. $\{011\}$ Type-I.1 twin interfaces via (c) HRSTEM and (d) DFT simulation. Zone axis is along $[100]$ for all images.

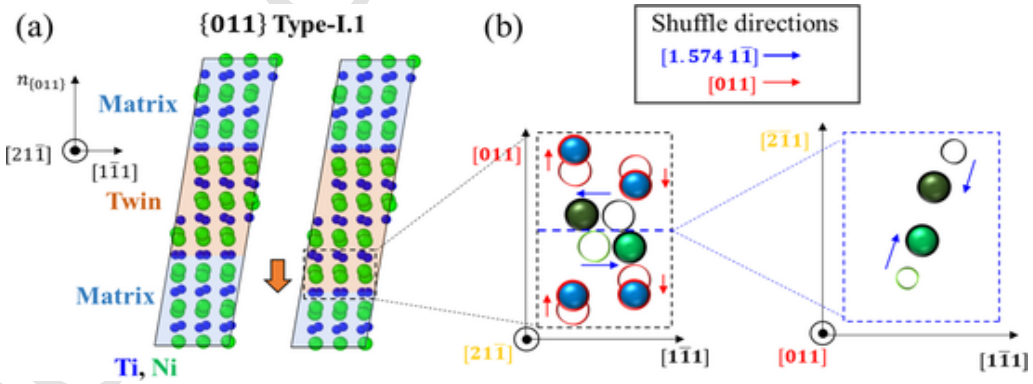

Fig. 11. Determination of atomic shuffles upon twin migration ($\{011\}$ Type-I.1 for example): (a) Schematic of twin migration, (b) Directions of atomic shuffle on lattice-motifs (Ti and Ni atoms).

formed because the results are MD potential dependent. The research reviews several MD potentials, including recent ones, and finds that the true energy minimum may be missed, often leading to an incorrect construction of twin interfaces.

The modeling results are compared to experimental HRSTEM experiments, and the model in this study correctly predicts the deviation of the twin surfaces from perfect reflective symmetry. In fact, the atom positions are captured within sub-angstrom resolution, and the periodicity of atomic waviness is in excellent agreement between theory and model. The results indicate that the HRSTEM magnifications required to resolve these displacements are higher than those used in previous studies. Subsequently, the twin migration was studied, and the unstable twin boundary energies were determined. These GPFE calculations rely heavily on the initial twin interface structure that is the starting point for such simulations.

We propose a hypothesis that the TB energy correlates with the atomic density at the interface (see Appendix C). For example, when comparing the atomic density in $\left\{11\bar{1}\right\}$ versus $\left\{34\bar{4}\right\}$ planes, the TB en-

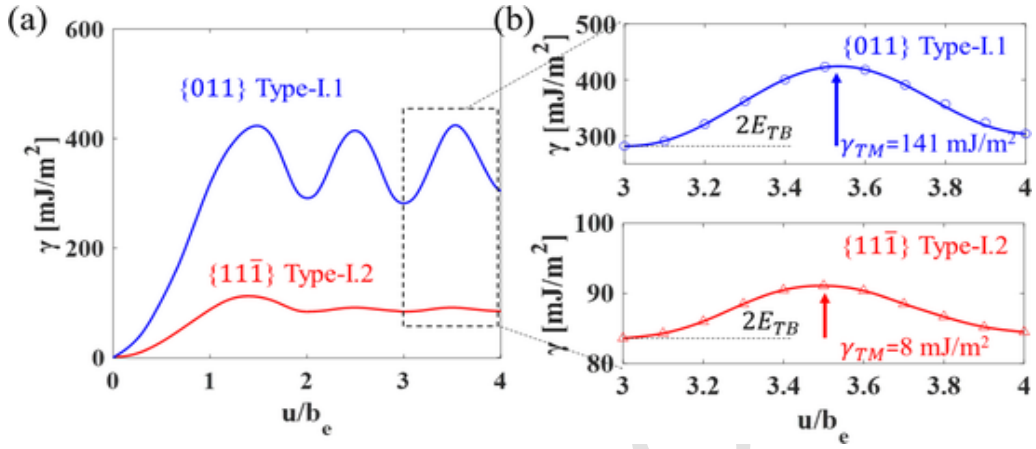

Fig. 12. Generalized planar fault energy (GPFE) curves of Type-I twinning modes in NiTi martensite. (a) Conjugate $\{011\}$ Type-I.1 and non-conjugate $\left\{11\bar{1}\right\}$ Type-I.2 twinning modes are compared in both nucleation and migration energy barriers. (b) Enlarged view of migration energy barriers.

Table 6
Energetics of different twinning modes in NiTi martensite.

Twinning mode	$b_e = sd$ [Å]	Twin nucleation, γ_{ut} [mJ/m^2]	Twin migration, γ_{TM} [mJ/m^2]	Twin stacking-fault energy, γ_{tsf} [mJ/m^2]	Ref.
$\{011\}$ Type-I.1 (*Conjugate*)	0.855	423	141	282	This study, DFT
$\left\{11\bar{1}\right\}$ Type-I.2 (*Non-conjugate*)	0.681	112	8	84	This study, DFT
$\langle 011\rangle$ Type-II.1 (*Conjugate*)	0.707	530	14	250	Ezaz & Sehitoglu, DFT

ergy for the $\left\{11\bar{1}\right\}$ interface was lower, corresponding to a higher atomic density (Fig. C1). Returning to our study, we evaluate the atomic density in $\left\{11\bar{1}\right\}$ and $\{011\}$ planes and find that the densities are 0.160 Å^{-2} and 0.111 Å^{-2}, respectively. The higher planar density in $\left\{11\bar{1}\right\}$ indeed corresponds to a lower TB energy 42 mJ/m^2, as compared to 141 mJ/m^2 in $\{011\}$. This finding is also consistent with the lower stacking fault energy in the $\{111\}$ plane compared to the $\{001\}$ plane in FCC, and higher density is well known for the $\{111\}$ FCC is the preferred slip system.

In this paper, we primarily focused on the significance of Type-I twinning modes in isolation. We are not considering Type-I/Type-II interactions that can lead to several modified interfaces. Recent work identifies four types of characteristic interfaces, and admittedly, these involve complex atomic arrangements [27,28]. While these experimental findings by one of the co-authors are well recognized, further atomistic understanding and analysis of energy barriers are left for future studies.

4. Conclusion

1. The TB energies for the Type-I twin in NiTi martensite varies widely depending on the MD potential and the omission of the "lattice offset" consideration to minimize the total energy. The current study circumvented the previous shortcomings upon consideration of lattice-offsets and subsequent twin migration through DFT calculations. The MD calculations of $\left\{11\bar{1}\right\}$ Type-I were in the range 75–210 mJ/m^2 while the correct theory results in this study are near 42 mJ/m^2.
2. If the lattice offsets are not included or incorrectly calculated, the electron diffraction patterns obtained from the twin interfaces create extra spots that do not conform to the experimental results. This is clear indication that previous works missed the correct structure of the Type-I TBs.
3. The corrugated twin interfaces are compared to experimental HRSTEM measurements, and the specific atoms at the interfaces were identified, and the model precisely predicts their locations.
4. The results have implications for understanding the growth of TBs and the recoverability in shape memory materials. Higher-order twin arrangements are also possible and left for future studies.

CRediT authorship contribution statement

Daegun You: Writing – review & editing, Writing – original draft, Visualization, Validation, Software, Methodology, Investigation, Formal analysis, Data curation, Conceptualization. **Ahmed Sameer Khan Mohammed:** Writing – review & editing, Software, Methodology, Data curation, Conceptualization. **Minoru Nishida:** Writing – review & editing, Visualization, Resources, Data curation, Conceptualization. **Huseyin Sehitoglu:** Writing – review & editing, Writing – original draft, Supervision, Resources, Project administration, Funding acquisition, Conceptualization.

Declaration of competing interest

The authors declare that they have no known competing financial interests or personal relationships that could have appeared to influence the work reported in this paper.

Acknowledgement

The work is supported by NSF DMR grants 2104971 and 2516016, which are gratefully acknowledged. Prof. Nishida acknowledges JSPS KAKENHI Grant Number 19H00829. This research was also supported in part by the Illinois Computes project which is supported by the University of Illinois Urbana-Champaign and the University of Illinois System. This research used the Delta advanced computing and data resource. Delta is a joint effort of the University of Illinois Urbana-

Champaign and its National Center for Supercomputing Applications (NCSA). The authors would also like to thank NCSA at the University of Illinois, and the Illinois Campus Cluster Program (ICCP) for their support. The authors thank Prof. M. Mitsuhara of Kyushu University for his skillful help with STEM observations.

Supplementary materials

Supplementary material associated with this article can be found, in the online version, at doi:10.1016/j.actamat.2025.121645.

Appendix A. Non-conjugate $\{11\bar{1}\}$ Type-I TB structure

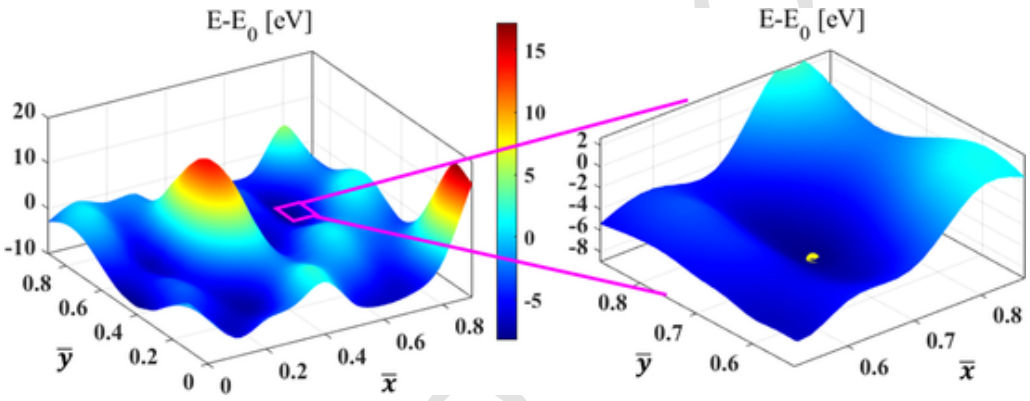

Fig. A1. Determination of lattice-offset for non-conjugate $\{11\bar{1}\}$ Type-I.2 TB structure: (E is the potential energy at a general offset $(\bar{x}, \bar{y})$ and E_0 is the energy at offset (0, 0), no offset, but $\bar{z} = 0.103$).

At incremental magnitudes of both $(\bar{x}, \bar{y})$ between 0 and 1, an DFT-SCF calculation is performed to determine the static energy of the atomic-structure at each offset in Fig. A1. The optimum lattice-offsets were found at (0.698, 0.703). The $\{11\bar{1}\}$ Type-I.2 TB structure is then fully relaxed including cell to obtain the TB energy. The resultant $\{11\bar{1}\}$ Type-I.2 twin configuration is depicted below in Fig. A2. Energy landscapes based on MD potentials are given in **Fig. S6–8** in the Supplementary materials.

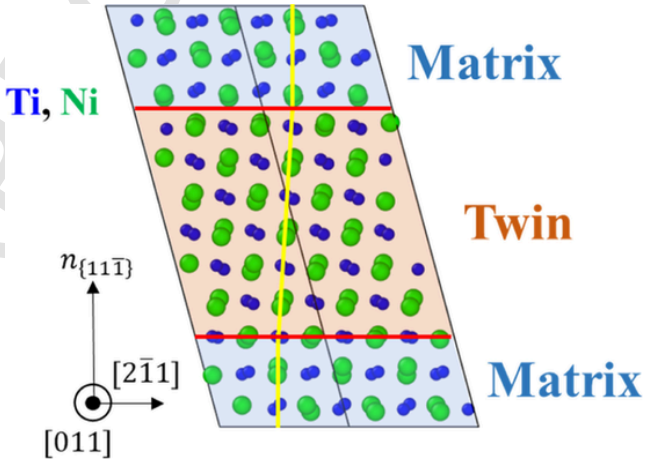

Fig. A2. Extended periodic simulation box of $\{11\bar{1}\}$ Type-I.2.

Appendix B. Experimental procedure

The Ti-50.0 at %Ni alloy was prepared from 99.7 mass % sponge Ti and 99.9 mass % electrolytic Ni by a high-frequency vacuum induction furnace using a graphite crucible, followed by casting into an iron mold. The ingot was hot-forged and cold-drawn into a rod 3 mm in diameter, which was sliced into disks 0.2 mm thick. The disks were solution-treated in vacuum at 1073 K for 3.6 ks, and then quenched into ice-water. The transformation temperatures were measured by differential scanning calorimetry (DSC). The Ms and Mf temperatures were 346 and 320 K, respectively. The average grain size of the parent B2 phase is estimated to be about 25 μm. The disks were mechanically polished to remove the surface scale. Subsequently, they were electropolished by the twin-jet method in an electrolyte solution of HNO3 and CH3OH (1:3, v/v) at about 240 K. Transmission

electron microscopy (TEM) and scanning transmission electron microscopy (STEM) observations were performed on aberration-corrected S/TEM systems (JEM-ARM200F, JEOL, operated at 200 kV and Titan G2 Cubed, Thermo Fischer Scientific, operated at 300 kV). A high-angle annular dark field (HAADF) detector with a detection angle range of 57–200 mrad was used to visualize the atomic arrangements in the twin boundary. Intensity profiles in atomic arrangements are exported by digital micrograph.

Appendix C. Planar density and TB energy

Fig. C1

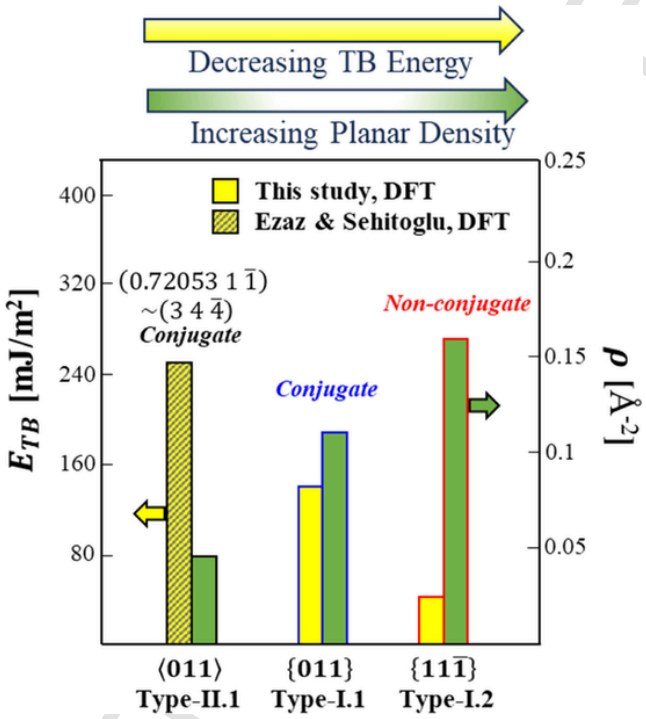

Fig. C1. Twin boundary (TB) energies, E_{TB}, of representative twinning modes in NiTi martensite compared to planar density, ρ, the number of atoms per unit plane area. The Type-I.2 boundary has the highest interplanar density and lowest twin boundary energy.

Representative twinning modes in NiTi martensite Type-I.1, Type-I.2, and Type-II.1 are subjected to the comparison between TB energies and planar density. The planar density, ρ, for each case calculates the number of atoms per unit plane area. For $\langle 011 \rangle$ Type-II.1 twinning mode, irrational plane $\left(0.72053\ 1\ \bar{1}\right)$ is approximated to $\left(34\bar{4}\right)$ plane to obtain planar density.

References

[1] K. Otsuka, C.M. Wayman, Shape Memory Materials, Cambridge university press, 1999.
[2] J.A. Shaw, S. Kyriakides, Thermomechanical aspects of NiTi, J. Mech. Phys. Solids 43 (8) (1995) 1243–1281.
[3] K. Otsuka, X. Ren, Physical metallurgy of Ti–Ni-based shape memory alloys, Prog. Mater. Sci. 50 (5) (2005) 511–678.
[4] K. Yamauchi, I. Ohkata, K. Tsuchiya, S. Miyazaki, Shape Memory and Superelastic alloys: Applications and Technologies, Elsevier, 2011.
[5] D.J. Hartl, D.C. Lagoudas, Aerospace applications of shape memory alloys, Proc. Inst. Mech. Eng. G: J. Aerosp. Eng. 221 (4) (2007) 535–552.
[6] J.M. Jani, M. Leary, A. Subic, M.A. Gibson, A review of shape memory alloy research, applications and opportunities, Mater. Des. 56 (2014) 1078–1113.
[7] T.W. Duerig, K. Melton, D. Stöckel, Engineering Aspects of Shape Memory Alloys, Butterworth-Heinemann, 2013.
[8] G. Olson, M. Cohen, Stress-assisted isothermal martensitic transformation: application to TRIP steels, Metall. Trans. A 13 (11) (1982) 1907–1914.
[9] K. Bhattacharya, Microstructure of martensite: Why It Forms and How It Gives Rise to the Shape-Memory Effect, Oxford University Press, 2003.
[10] A.S.K. Mohammed, H. Sehitoglu, Thermodynamic rationale for transformation-induced dislocations in shape memory alloys, Acta Mater. 274 (2024) 119998.
[11] J. Wang, H. Sehitoglu, Twinning stress in shape memory alloys: theory and experiments, Acta Mater. 61 (18) (2013) 6790–6801.
[12] J. Wang, H. Sehitoglu, Dislocation slip and twinning in Ni-based L12 type alloys, Intermetallics 52 (2014) 20–31.
[13] J. Wang, H. Sehitoglu, Martensite modulus dilemma in monoclinic NiTi-theory and experiments, Int. J. Plast. 61 (2014) 17–31.
[14] A.S.K. Mohammed, H. Sehitoglu, Martensitic twin boundary migration as a source of irreversible slip in shape memory alloys, Acta Mater. 186 (2020) 50–67.
[15] A.S.K. Mohammed, H. Sehitoglu, Modeling the interface structure of type II twin boundary in B19′ NiTi from an atomistic and topological standpoint, Acta Mater. 183 (2020) 93–109.
[16] A.S.K. Mohammed, H. Sehitoglu, Strain-sensitive topological evolution of twin interfaces, Acta Mater. 208 (2021) 116716.
[17] T. Ezaz, H. Sehitoglu, Type II detwinning in NiTi, Appl. Phys. Lett. 98 (14) (2011) 141906.
[18] T. Ezaz, H. Sehitoglu, H. Maier, Energetics of twinning in martensitic NiTi, Acta Mater. 59 (15) (2011) 5893–5904.
[19] T. Ezaz, H. Sehitoglu, H.J. Maier, Energetics of (114) twinning in B2 NiTi under coupled shear and shuffle, Acta Mater. 60 (1) (2012) 339–348.
[20] J. Wang, H. Sehitoglu, Modeling of pseudotwinning in Fe3Ga, Model. Simul. Mater. Sci. Eng. 22 (5) (2014) 055008.
[21] J. Wang, H. Sehitoglu, Modelling of martensite slip and twinning in NiTiHf shape memory alloys, Philos. Mag. 94 (20) (2014) 2297–2317.
[22] K. Yamauchi, M. Nishida, I. Itai, K. Kitamura, A. Chiba, Specimen preparation for transmission electron microscopy of twins in B19′ Martensite of Ti-Ni shape memory alloys, Mater. Trans. JIM 37 (3) (1996) 210–217.
[23] M. Nishida, H. Ohgi, I. Itai, A. Chiba, K. Yamauchi, Electron microscopy studies of twin morphologies in B19′ martensite in the Ti-Ni shape memory alloy, Acta Metall. Mater. 43 (3) (1995) 1219–1227.
[24] S.P. Gupta, A.A. Johnson, Morphology and crystallography of β' Martensite in TiNi alloys, Trans. Jpn. Inst. Met. 14 (4) (1973) 292–302.
[25] M. Krishnan, J.B. Singh, A novel B19′ martensite in nickel titanium shape memory alloys, Acta Mater. 48 (6) (2000) 1325–1344.
[26] M. Nishida, T. Hara, M. Matsuda, S. Ii, Crystallography and morphology of

various interfaces in Ti–Ni, Ti–Pd and Ni–Mn–Ga shape memory alloys, Mater. Sci. Eng.: A 481–482 (2008) 18–27.
[27] M. Nishida, T. Nishiura, H. Kawano, T. Inamura, Self-accommodation of B19′ martensite in Ti–Ni shape memory alloys–Part I. Morphological and crystallographic studies of the variant selection rule, Philos. Mag. 92 (17) (2012) 2215–2233.
[28] M. Nishida, E. Okunishi, T. Nishiura, H. Kawano, T. Inamura, S. Ii, T. Hara, Self-accommodation of B19′ martensite in Ti–Ni shape memory alloys – Part II. Characteristic interface structures between habit plane variants, Philos. Mag. 92 (17) (2012) 2234–2246.
[29] T. Onda, Y. Bando, T. Ohba, K. Otsuka, Electron microscopy study of twins in martensite in a Ti-50.0 at%Ni alloy, Mater. Trans. JIM 33 (4) (1992) 354–359.
[30] T. Inamura, T. Nishiura, H. Kawano, H. Hosoda, M. Nishida, Self-accommodation of B19′ martensite in Ti–Ni shape memory alloys. Part III. Analysis of habit plane variant clusters by the geometrically nonlinear theory, Philos. Mag. 92 (17) (2012) 2247–2263.
[31] G. Ren, H. Sehitoglu, Interatomic potential for the NiTi alloy and its application, Comput. Mater. Sci. 123 (2016) 19–25.
[32] W.-S. Ko, B. Grabowski, J. Neugebauer, Development and application of a Ni-Ti interatomic potential with high predictive accuracy of the martensitic phase transition, Phys. Rev. B 92 (13) (2015) 134107.
[33] H. Tang, Y. Zhang, Q.-J. Li, H. Xu, Y. Wang, Y. Wang, J. Li, High accuracy neural network interatomic potential for NiTi shape memory alloy, Acta Mater. 238 (2022) 118217.
[34] B.A. Bilby, A.G. Crocker, The theory of the crystallography of deformation twinning, Proc. R. Soc. Lond., A. Math. Phys. Sci. R. Soc. (1965) 240–255.
[35] J.W. Christian, S. Mahajan, Deformation twinning, Prog. Mater. Sci. 39 (1) (1995) 1–157.
[36] I.J. Beyerlein, X. Zhang, A. Misra, Growth twins and deformation twins in metals, Annu Rev. Mater. Res. 44 (1) (2014) 329–363.
[37] Q. Zhu, Q. Huang, Y. Tian, S. Zhao, Y. Chen, G. Cao, K. Song, Y. Zhou, W. Yang, Z. Zhang, X. An, H. Zhou, J. Wang, Hierarchical twinning governed by defective twin boundary in metallic materials, Sci. Adv. 8 (20) (2022) eabn8299.
[38] O. Heczko, Understanding motion of twin boundary—A key to magnetic shape memory effect, IEEE Trans. Magn. 50 (11) (2014) 1–7.
[39] N. Zou, Z. Li, Y. Zhang, B. Yang, X. Zhao, C. Esling, L. Zuo, Plastic deformation of Ni–Mn–Ga 7M modulated martensite by twinning & detwinning and intermartensitic transformation, Int. J. Plast. 100 (2018) 1–13.
[40] K.M. Knowles, D.A. Smith, The crystallography of the martensitic transformation in equiatomic nickel-titanium, Acta Metall. 29 (1) (1981) 101–110.
[41] K.M. Knowles, A high-resolution electron microscope study of nickel-titanium martensite, Philos. Mag. A 45 (3) (1982) 357–370.
[42] Y. Liu, Z.L. Xie, Twinning and detwinning of ⟨011⟩ type II twin in shape memory alloy, Acta Mater. 51 (18) (2003) 5529–5543.
[43] Z.L. Xie, Y. Liu, HRTEM study of ⟨011⟩ type II twin in NiTi shape memory alloy, Philos. Mag. 84 (32) (2004) 3497–3507.
[44] R.C. Pond, J.P. Hirth, K.M. Knowles, Topological model of type II deformation twinning in NiTi martensite, Philos. Mag. 99 (13) (2019) 1619–1632.
[45] M. Matsuda, K. Kuramoto, Y. Morizono, S. Tsurekawa, E. Okunishi, T. Hara, M. Nishida, Transmission electron microscopy of antiphase boundary-like structure of B19′ martensite in Ti–Ni shape memory alloy, Acta Mater. 59 (1) (2011) 133–140.
[46] M. Nishida, K. Yamauchi, I. Itai, H. Ohgi, A. Chiba, High resolution electron microscopy studies of twin boundary structures in B19′ martensite in the Ti-Ni shape memory alloy, Acta Metall. Mater. 43 (3) (1995) 1229–1234.
[47] K. Otsuka, T. Sawamura, K. Shimizu, Crystal structure and internal defects of equiatomic TiNi martensite, Phys. Status Solidi A 5 (2) (1971) 457.
[48] M. Nishida, C.M. Wayman, A. Chiba, Electron microscopy studies of the martensitic transformation in an aged Ti-51at%Ni shape memory alloy, Metallography 21 (3) (1988) 275–291.
[49] H. Sehitoglu, R. Hamilton, D. Canadinc, X.Y. Zhang, K. Gall, I. Karaman, Y. Chumlyakov, H.J. Maier, Detwinning in NiTi alloys, Metall. Mater. Trans. A 34 (1) (2003) 5–13.
[50] H. Sehitoglu, I. Karaman, R. Anderson, X. Zhang, K. Gall, H.J. Maier, Y. Chumlyakov, Compressive response of NiTi single crystals, Acta Mater. 48 (13) (2000) 3311–3326.
[51] O. Matsumoto, S. Miyazaki, K. Otsuka, H. Tamura, Crystallography of martensitic transformation in Ti-Ni single crystals, Acta Metall. 35 (8) (1987) 2137–2144.
[52] S. Miyazaki, K. Otsuka, Y. Suzuki, Transformation pseudoelasticity and deformation behavior in a Ti-50.6at%Ni alloy, Scr. Metall. 15 (3) (1981) 287–292.
[53] T. Waitz, V. Kazykhanov, H. Karnthaler, Martensitic phase transformations in nanocrystalline NiTi studied by TEM, Acta Mater. 52 (1) (2004) 137–147.
[54] T. Waitz, D. Spišák, J. Hafner, H. Karnthaler, Size-dependent martensitic transformation path causing atomic-scale twinning of nanocrystalline NiTi shape memory alloys, EPL (Europhys. Lett.) 71 (1) (2005) 98.
[55] M. Nishida, S. Ii, K. Kitamura, T. Furukawa, A. Chiba, T. Hara, K. Hiraga, New deformation twinning mode of B19′ martensite in Ti-Ni shape memory alloy, Scr. Mater. 39 (12) (1998) 1749–1754.
[56] D.S. Lieberman, M. Wechsler, T. Read, Cubic to orthorhombic diffusionless phase change—Experimental and theoretical studies of AuCd, J. Appl. Phys. 26 (4) (1955) 473–484.
[57] J. Bowles, J. Mackenzie, The crystallography of martensite transformations I, Acta Metall. 2 (1) (1954) 129–137.
[58] C.M. Wayman, Introduction to the Crystallography of Martensitic Transformations, Macmillan, 1964.
[59] J.W. Christian, The Theory of Transformations in Metals and Alloys, Newnes, 2002.
[60] L. La Rosa, F. Maresca, Atomistic simulations of structure and motion of twin interfaces reveal the origin of twinning in NiTi shape memory alloys, Commun. Mater. 5 (1) (2024) 142.
[61] K. Adachi, J. Perkins, C.M. Wayman, Type II twins in self-accommodating martensite plate variants in a Cu-Zn-Al shape memory alloy, Acta Metall. 34 (12) (1986) 2471–2485.
[62] T. Hara, T. Ohba, S. Miyazaki, K. Otsuka, Electron microscopy study of type II twins in γ_1' Cu-Al-Ni martensite, Mater. Trans. JIM 33 (12) (1992) 1105–1113.
[63] Y. Murakami, K. Otsuka, S. Hanada, S. Watanabe, Self-accomodation and morphology of 14M (7R) martensites in an Ni-37.0at.%Al alloy, Mater. Sci. Eng.: A 189 (1) (1994) 191–199.
[64] M. Nishida, T. Hara, Y. Morizono, A. Ikeya, H. Kijima, A. Chiba, Transmission electron microscopy of twins in martensite in Ti-Pd shape memory alloy, Acta Mater. 45 (11) (1997) 4847–4853.
[65] Y. Zhong, K. Gall, T. Zhu, Atomistic study of nanotwins in NiTi shape memory alloys, J. Appl. Phys. 110 (3) (2011) 033532.
[66] M. Muralles, S.-D. Park, S.Y. Kim, B. Lee, Phase transformations, detwinning and superelasticity of shape-memory NiTi from MEAM with practical capability, Comput. Mater. Sci. 130 (2017) 138–143.
[67] Y.-K. Kim, H.-K. Kim, W.-S. Jung, B.-J. Lee, Development and application of Ni-Ti and Ni-Al-Ti 2NN-MEAM interatomic potentials for Ni-base superalloys, Comput. Mater. Sci. 139 (2017) 225–233.
[68] D. You, A.S.K. Mohammed, H. Sehitoglu, Direct comparison of molecular dynamics models for superelasticity in NiTi, Shape Mem. Superelasticity (2025).
[69] G. Kresse, J. Furthmüller, Efficient iterative schemes for ab initio total-energy calculations using a plane-wave basis set, Phys. Rev. B 54 (16) (1996) 11169–11186.
[70] G. Kresse, D. Joubert, From ultrasoft pseudopotentials to the projector augmented-wave method, Phys. Rev. B 59 (3) (1999) 1758–1775.
[71] J.P. Perdew, K. Burke, M. Ernzerhof, Generalized gradient approximation made simple, Phys. Rev. Lett. 77 (18) (1996) 3865–3868.
[72] A.P. Thompson, H.M. Aktulga, R. Berger, D.S. Bolintineanu, W.M. Brown, P.S. Crozier, P.J. in 't Veld, A. Kohlmeyer, S.G. Moore, T.D. Nguyen, R. Shan, M.J. Stevens, J. Tranchida, C. Trott, S.J. Plimpton, LAMMPS - a flexible simulation tool for particle-based materials modeling at the atomic, meso, and continuum scales, Comput. Phys. Commun. 271 (2022) 108171.
[73] A. Stukowski, Visualization and analysis of atomistic simulation data with OVITO–the Open Visualization Tool, Model. Simul. Mater. Sci. Eng. 18 (1) (2010) 015012.
[74] A.S.K. Mohammed, H. Sehitoglu, Structural characteristics of irrational type-II Twin interfaces, Int. J. Plast. 178 (2024) 104016.
[75] D. You, O.K. Celebi, G. Gengor, A.S.K. Mohammed, W. Abuzaid, H. Sehitoglu, Short-range ordering mechanics in FCC materials, Int. J. Plast. 174 (2024) 103919.
[76] E. Goo, R. Sinclair, The B2 to R transformation in Ti50Ni47Fe3 and Ti49.5Ni50.5 alloys, Acta Metall. 33 (9) (1985) 1717–1723.
[77] X. Huang, G.J. Ackland, K.M. Rabe, Crystal structures and shape-memory behaviour of NiTi, Nat. Mater. 2 (5) (2003) 307–311.
[78] Y. Kudoh, M. Tokonami, S. Miyazaki, K. Otsuka, Crystal structure of the martensite in Ti-49.2 at.%Ni alloy analyzed by the single crystal X-ray diffraction method, Acta Metall. 33 (11) (1985) 2049–2056.
[79] B. Li, Y. Shen, Q. An, Structural origin of reversible martensitic transformation and reversible twinning in NiTi shape memory alloy, Acta Mater. 199 (2020) 240–252.
[80] G. Gengor, A.S.K. Mohammed, H. Sehitoglu, {101¯2} Twin interface structure and energetics in HCP materials, Acta Mater. 219 (2021) 117256.
[81] G. Gengor, A.S.K. Mohammed, H. Sehitoglu, The complexity of {112¯1} twin interface structure and energetics in HCP materials, Acta Mater. 255 (2023) 119040.
[82] H. Sehitoglu, G. Anlas, A.S.K. Mohammed, Shape Memory alloys – Frontier Developments, Eds., in: M.H.F. Aliabadi, W.O. Soboyejo (Eds.), Comprehensive Structural Integrity, 2nd Edition, Elsevier, Oxford, 2023, pp. 610–679.
[83] P. Chowdhury, H. Sehitoglu, Deformation physics of shape memory alloys – Fundamentals at atomistic frontier, Prog. Mater. Sci. 88 (2017) 49–88.
[84] P. Chowdhury, H. Sehitoglu, A revisit to atomistic rationale for slip in shape memory alloys, Prog. Mater. Sci. 85 (2017) 1–42.
[85] M.S. Wechsler, D.S. Lieberman, T.A. Read, On theory of formation of martensite, J. Met. 5 (11) (1953) 1503–1515.
[86] X. Zhang, H. Sehitoglu, Crystallography of the B2 → R → B19′ phase transformations in NiTi, Mater. Sci. Eng.: A 374 (1) (2004) 292–302.